

Deep Learning-based MRI Reconstruction with Artificial Fourier Transform Network (AFTNet)

Yanting Yang^a, Yiren Zhang^a, Zongyu Li^a, Jeffery Siyuan Tian^b, Matthieu Dagommer^a, Jia Guo^c

^a*Department of Biomedical Engineering, Columbia University, 500 W. 120th Street
#351, New York, 10027, NY, United States*

^b*Department of Computer Science, University of Maryland, 8125 Paint Branch
Drive, College Park, 20742, MD, United States*

^c*Department of Psychiatry, Columbia University, 1051 Riverside Drive, New
York, 10032, NY, United States*

Abstract

Deep complex-valued neural networks provide a powerful way to leverage complex number operations and representations and have succeeded in several phase-based applications. However, most previously published networks have not fully explored the impact of complex-valued networks in the frequency domain. Here, we introduce a unified complex-valued deep learning framework—Artificial Fourier Transform Network (AFTNet)—which combines domain-manifold learning and complex-valued neural networks. AFTNet can be readily used to solve image inverse problems in domain transformation, especially for accelerated magnetic resonance imaging (MRI) reconstruction and other applications. While conventional methods only accept magnitude images, the proposed method takes raw k-space data in the frequency domain as input, allowing a mapping between the k-space and image domains to be determined through cross-domain learning. We show that AFTNet achieves superior accelerated MRI reconstruction compared to existing approaches. Furthermore, our approach can be applied to various tasks, such as denoised magnetic resonance spectroscopy (MRS) reconstruction and datasets with various contrasts. The AFTNet presented here is a valuable preprocessing component for different preclinical studies and provides an innovative alternative for solving inverse problems in imaging and spectroscopy.

Email address: jg3400@columbia.edu (Jia Guo)

The code is available at: <https://github.com/yanting-yang/AFT-Net>.

Keywords: MRI, Deep Learning, Reconstruction

1. Introduction

The shift from real to complex coordinate space in deep neural networks has revealed the potential of complex numbers' rich representational capacity, thereby advancing the development of complex-valued neural architectures[1, 2, 3]. A similar but inverse domain shift occurs in the preprocessing of magnetic resonance imaging (MRI), where raw data are acquired and stored in complex-valued k-space, with each pixel representing the spatial frequency information in two or three dimensions of an object. After data acquisition, the raw k-space data are transformed into images through the image reconstruction process, enabling interpretation by MR operators, physicians, radiologists, or data scientists. This reconstruction is an essential step in the preprocessing pipeline and lays the foundation for overall image quality. Proper image reconstruction methods can increase the signal-to-noise ratio (SNR) by removing thermal noise[4, 5], improve spatial inhomogeneities affected by point spread functions (PSFs), and correct unexpected signal artifacts[6].

Theoretically, image data are reconstructed by domain transforms—for example, Fourier transforms for fully sampled Cartesian data[7]. However, under conditions of signal nonideality commonly encountered in clinical acquisitions, numerical and machine-learning methods are required. Human experts are involved in selecting task-related features and establishing models that accurately represent the mapping between the k-space and image domains[8], including methods such as Fast Fourier Transform (FFT)[9], noise prewhitening[6], digital signal processing (DSP), interpolation, and coil combination. Nevertheless, due to significant pathological variations and the potential for human oversight[10], a consistent and unbiased diagnosis cannot be guaranteed. In recent years, k-space, as a low-dimensional feature space, has been leveraged in deep neural networks to learn the manifold mapping of domain transforms in low signal-to-noise settings[11]. This image reconstruction process can be reformulated as a data-driven supervised learning task that determines the mapping between the k-space and image domains, demonstrating superior immunity to noise and reconstruction artifacts. The conventional discrete Fourier transform algorithm, which is mathematically

derived and not based on learning, can be substituted by neural networks[12]. Thus, fundamental neural networks have been presented that avoid the difficulties of network structure finding and algorithm optimization. A similar approach is adopted in domain-transform manifold learning along the phase-encoding direction[13], where front-end convolutional layers, an intermediate global transform, and back-end convolutional layers are combined to perform data restoration in both k-space and image domains. Modern score-based diffusion models provide a powerful way to sample data from a conditional distribution given the measurements in the k-space domain, which can be used to solve inverse problems in imaging[14].

While most deep learning-based MR image reconstruction algorithms have applied the concept of domain-transform learning that directly learns a low-dimensional joint manifold between the k-space and image domains, few works have fully leveraged complex-valued neural networks (CVNNs), which enable neural networks to implement learning-based frequency selection[15]. Some early works proposed CVNNs but mainly focused on solving the basics of learning[16, 17]. Extensive studies on complex-valued CNNs have been conducted in recent years. Generalizations of real-valued CNN models have been shown to be significantly less vulnerable to overfitting[2]. Mathematical arguments and implementations have also been discussed[18, 3], enabling the practical application of CVNNs. A combination of CVNNs and vision deep learning models (e.g., U-Net[19]) has recently emerged and is being exploited for MR image reconstruction[20, 21], demonstrating superior and accelerated reconstruction compared to real-valued neural networks. However, the main drawback of previous CVNN works is that the potential of leveraging CVNNs in domain manifold learning has not been fully investigated.

In this study, we combine domain-manifold learning with complex-valued neural networks to develop a unified end-to-end complex-valued image reconstruction approach for MRI. The framework we describe is the artificial Fourier transform network (AFTNet), as shown in Figure 1, which aims to facilitate the MR reconstruction with the presence of noise in k-space from the preprocessing workflow and incorporate data processing into deep learning frameworks. It consists of a trainable data-driven domain transformation block (AFT) that approximates the Fourier transform (FT) and complex-valued convolutional encoder-decoder networks to extract higher-level features in the k-space and image domains. Through its modular design, the proposed AFTNet can be extended to any dimension (e.g., 1D MR spectroscopy data). We use AFTNet to accelerate and denoise MR acquisitions.

In accelerated MRI reconstruction, the k-space data are under-sampled in the data acquisition direction (the phase-encoding direction). We further apply the extended AFTNet to denoised MRS acquisition, where the free induction decay (FID) data are under-sampled by decreasing repetition numbers. Comprehensive experiments are conducted across various modalities, system field strengths, acceleration ratios, and noise levels.

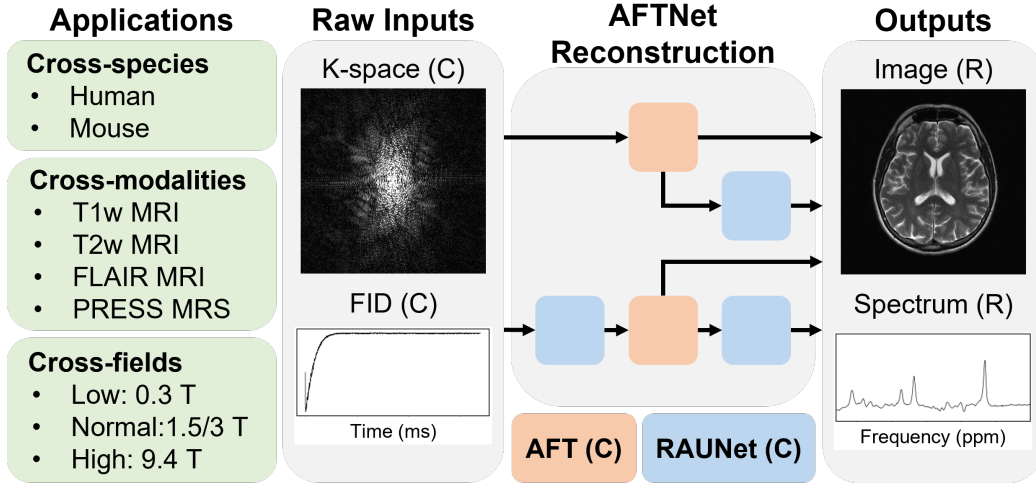


Figure 1: Schematics of general deep-learning MR imaging/spectroscopy reconstruction based on AFTNet. The generality of AFTNet is evaluated on the human normal-field MRI dataset (fastMRI[22]) and human normal-field MRS dataset (Big GABA[23]). The inputs of AFTNet can be 2D MRI k-space data or 1D MRS FID data. The outputs are reconstructed MR images or spectra. Different structures of AFTNet are developed by appending front-end and/or back-end convolutional networks to the AFT block. Here we show the human T2w 1.5T MRI and human 3T PRESS MRS reconstruction results, respectively. C: complex-valued and R: real-valued.

2. Background

2.1. Complex-valued neural network

The definition of the conventional real-valued neural network can be extended to the complex domain. We denote a complex operator as $W = W_{real} + iW_{imag}$, where W_{real} and W_{imag} are real-valued operators. The input complex vector can be represented as $x = x_{real} + ix_{imag}$. The output of

complex operator W acting on x is derived following the vector dot product:

$$\begin{aligned} y &= W * x \\ &= (W_{real}(x_{real}) - W_{imag}(x_{imag})) \\ &\quad + i(W_{imag}(x_{real}) + W_{real}(x_{imag})). \end{aligned} \tag{1}$$

As the linear operator and convolution operator are distributive[3], we obtain:

$$\begin{aligned} \mathbb{C}\text{Linear}(z) &= (\text{Linear}_1(\Re(z)) - \text{Linear}_2(\Im(z))) \\ &\quad + i(\text{Linear}_2(\Re(z)) + \text{Linear}_1(\Im(z))) \end{aligned} \tag{2}$$

and

$$\begin{aligned} \mathbb{C}\text{Conv}(z) &= (\text{Conv}_1(\Re(z)) - \text{Conv}_2(\Im(z))) \\ &\quad + i(\text{Conv}_2(\Re(z)) + \text{Conv}_1(\Im(z))) \end{aligned} \tag{3}$$

where $z \in \mathbb{C}$ and we use subscripts 1 and 2 instead of *real* and *imag* to avoid misleading.

The complex version of the ReLU activation function we used in this study simply applies separate ReLU on both the real and the imaginary part of the input as follows:

$$\mathbb{C}\text{ReLU}(z) = \text{ReLU}(\Re(z)) + i\text{ReLU}(\Im(z)) \tag{4}$$

which satisfies Cauchy–Riemann equations[3] when both the real and the imaginary parts have the same sign or $\theta_z \in [0, \frac{1}{2}\pi] \cup [\pi, \frac{3}{2}\pi]$.

Normalization is a common technique widely used in deep learning to accelerate training and reduce statistical covariance shift[24, 25, 26]. This is also mirrored in the complex-valued neural network, where we want to ensure that both the real and the imaginary parts have equal variance. Extending the normalization equation to matrix notation we have:

$$\tilde{z} = V^{-\frac{1}{2}}(z - \mathbb{E}(z)) \tag{5}$$

where $x - \mathbb{E}(x)$ simply zero centers the real and the imaginary parts separately

$$z - \mathbb{E}(z) = \begin{bmatrix} \Re(z) - \text{Mean}(\Re(z)) \\ \Im(z) - \text{Mean}(\Im(z)) \end{bmatrix} \tag{6}$$

and V is the covariance matrix of real and imaginary parts of z

$$\begin{aligned} V &= \begin{bmatrix} V_{rr} & V_{ri} \\ V_{ir} & V_{ii} \end{bmatrix} + \epsilon I \\ &= \begin{bmatrix} \text{Cov}(\Re(z), \Re(z)) & \text{Cov}(\Re(z), \Im(z)) \\ \text{Cov}(\Im(z), \Re(z)) & \text{Cov}(\Im(z), \Im(z)) \end{bmatrix} + \epsilon I. \end{aligned} \quad (7)$$

V is a 2×2 matrix, and the existence of the inverse square root is guaranteed by the addition of ϵI (Tikhonov regularization). Therefore, the solution of the inverse square root can be expressed analytically as

$$V = \begin{bmatrix} A & B \\ C & D \end{bmatrix} \Rightarrow V^{-\frac{1}{2}} = \begin{bmatrix} (D+s)/d & -B/d \\ -C/d & (A+s)/d \end{bmatrix} \quad (8)$$

where $s = \sqrt{AD - BC}$, $t = \sqrt{A + D + 2s}$ and $d = st$.

The complex normalization is defined as

$$\text{Norm}(z) = \gamma \tilde{z} + \beta = \begin{bmatrix} \gamma_{rr} & \gamma_{ri} \\ \gamma_{ri} & \gamma_{ii} \end{bmatrix} \tilde{z} + \begin{bmatrix} \Re(\beta) \\ \Im(\beta) \end{bmatrix}. \quad (9)$$

where γ and β are learnable parameters.

Considering the limitation of GPU RAM and large memory consumption of complex-valued networks, we use the group normalization[25] in our framework to avoid possible inaccurate batch statistics estimation caused by a small batch size. The group normalization in the complex domain can be represented as Algorithm 1.

Algorithm 1 Complex group normalization

Input: z, γ, β, G (number of groups), ϵ
Shape of z is (B, C, H, W)
Reshape z to $(B, G, C//G, H, W)$
for each group **do**
 $\tilde{z} \leftarrow V^{-\frac{1}{2}}(z - \mathbb{E}(z))$ based on Equations (6) to (8).
end for
Reshape \tilde{z} to (B, C, H, W)
return $\gamma \tilde{z} + \beta$

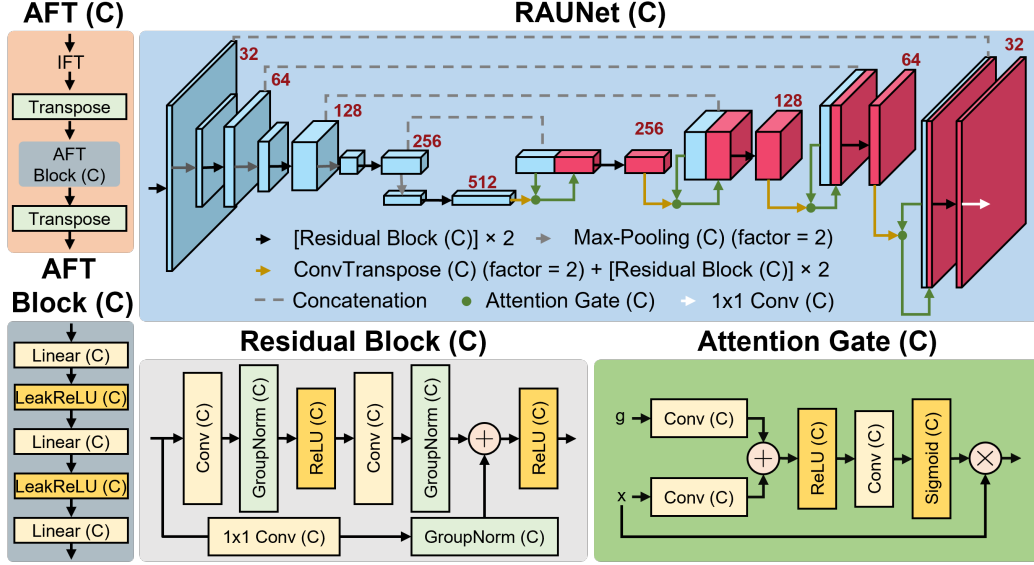


Figure 2: Structure of 2-dimensional AFTNet. Components include the complex-valued AFT block, the complex-valued residual attention U-Net, the complex-valued residual block, and the complex-valued attention gate. All convolutional layers have a kernel size of 3, except those pointed out specifically. C: complex-valued. Red numbers indicate the number of channels produced by each layer.

3. Methods

3.1. Artificial Fourier Transform

Take cartesian sampling which is widely used in conventional MRI acquisitions as an example, since 2D discrete Fourier transform (DFT) is a linear operation and can be represented by two successive 1D DFTs as

$$\begin{aligned} \mathcal{F}_{x,y}\{f(x,y)\} &= \mathcal{F}_x\{\mathcal{F}_y\{f(x,y)\}\} \\ &= \mathcal{F}_y\{\mathcal{F}_x\{f(x,y)\}\}, \end{aligned} \quad (10)$$

where the x and y are two separable independent variables. Each dimension of 2D DFT can be modeled as a trainable neural network[12]. We further proposed that this idea could be naturally implemented with complex-valued neural networks shown in Figure 2.

From the definition of the discrete Fourier transform of a sequence of N complex numbers which can be represented in the real and imaginary parts as

$$Z_k = \sum_{n=0}^{N-1} z_n \left[\cos\left(\frac{2\pi}{N}kn\right) - i \sin\left(\frac{2\pi}{N}kn\right) \right], \quad (11)$$

rewrite Equation (11) as

$$Z_k = W_{real}z + iW_{imag}z, \quad (12)$$

where W_{real} and W_{imag} are the real and the imaginary coefficients. Use matrix notation to represent real and imaginary parts of the DFT operation. We have:

$$\begin{bmatrix} \Re(Z_k) \\ \Im(Z_k) \end{bmatrix} = \begin{bmatrix} W_{real} & -W_{imag} \\ W_{imag} & W_{real} \end{bmatrix} \begin{bmatrix} \Re(z) \\ \Im(z) \end{bmatrix}. \quad (13)$$

Compare Equation (13) with Equation (1), a multi-layer complex-valued neural network with linear activation function can represent 1D DFT with appropriate weights. We use AFT_N to denote the complex-valued Fourier transform deep learning block on the input vector with N elements. The Fourier transform of the input data with dimension $H \times W$ can be represented as

$$Z = AFT_H(AFT_W(z)^T)^T. \quad (14)$$

3.2. Network framework

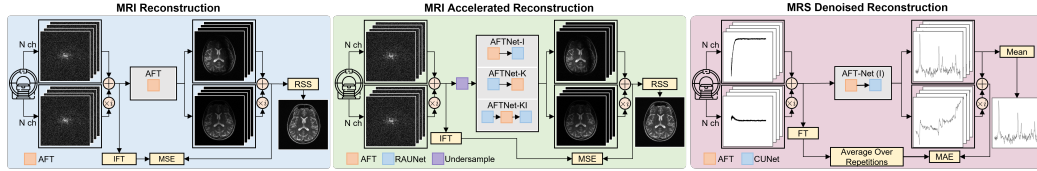


Figure 3: The workflows of experiments on each dataset.

The network structure and general workflow are shown in Figure 2 and Figure 3. The AFT block is composed of an MLP with three complex linear layers linked by two complex LeakReLU activation layers. We set the negative slope of LeakReLU to be 0.1. As for conventional accelerated MRI acquisition, the undersampling is applied to the phase-encoding direction, we also only apply the AFT block to that direction. We apply our AFT to the multi-coil k-space data acquired directly from the scanner for the reconstruction task. The target is derived from the inverse fast Fourier transform on the input data. The AFT does not compress the coil channel so that the input and output shapes/sizes are the same. The network performance is evaluated within magnitude images obtained by the Fourier application and coil compression. For the accelerated reconstruction task, we combine our AFT with an entirely complex-valued residual attention U-Net (RAUNet)[20], which

extracts local and global features in the k-space and/or image domain and forces the network to represent sparsely in those domains. Multiple network architectures are evaluated to verify the effectiveness of both AFT and RAUNet in different domains. We refer each of them to **AFT**, **AFTNet-I**, **AFTNet-K**, and **AFTNet-KI**, respectively as shown in Figure 3. We first train an AFT-only network to see if, without convolution layers, the AFT can remove artifacts and enhance quality. Then a network with the AFT followed by the RAUNet is trained to simulate a typical deep learning workflow where conventional numerical methods are used to preprocess the image, and CNNs are utilized to map the input domain to the target domain. We also evaluate the network with RAUNet first implemented directly on the k-space domain. Given that each position in k-space contains the information of the whole image, CNNs implemented in k-space can leverage the complete information of all space, even if they have a fixed field of view. Finally, a RAUNet-AFT-RAUNet structure is evaluated with the first RAUNet extracting k-space domain features and the second RAUNet extracting image domain features.

The architecture of the RAUNet presented in Figure 2 is generally based on the residual attention U-Net[19] but with all the real-valued components replaced by complex-valued components as shown in Figure 2, including complex-valued convolutional layers and complex-valued ReLU layers introduced in Section 2.1. We further optimize the network for smaller batch sizes by replacing batch normalization with group normalization as illustrated in Algorithm 1. Other complex components are implemented in the same way. For example, the complex transposed convolution operator can be mirrored from Equation (3), complex sigmoid is applied like complex ReLU, and complex max pooling is almost the same as the real-valued version except that indices are inferred from absolute values.

3.3. Implementation details

We construct a batch size of 1 and optimize the network using the ADAM[27] optimizer. We use a learning rate scheduler with cosine annealing[28]. The initial learning rate is 10^{-3} and the final learning rate is 10^{-5} . All methods are trained for 50 epochs. All experiments are done using PyTorch 2.2.2 and a Quadro RTX 6000 GPU.

In the context of image reconstruction and processing, the impact of the loss function is vital if the final results are to be evaluated by human observers. One common and safe choice is ℓ_2 loss which works under the assumption of white Gaussian noise. For training AFT for MRI reconstruction,

the loss value is determined in the frequency domain as

$$\mathcal{L}^{recon} = \mathcal{L}^{\ell_2}(\Re(x), \Re(y)) + \mathcal{L}^{\ell_2}(\Im(x), \Im(y)) \quad (15)$$

so that both real and imaginary outputs are optimized to match the conventional Fourier transformation. x and y are predicted and targeted complex-valued images. For training AFTNet for accelerated MRI reconstruction, we also want to minimize the error of magnitude images. Therefore, the loss value for accelerated MRI reconstruction is

$$\mathcal{L}^{acc} = \mathcal{L}^{recon} + \mathcal{L}^{\ell_2}(\text{RSS}(x), \text{RSS}(y)) \quad (16)$$

where the root-sum-of-squares (RSS) approach[29] is applied to complex-valued output from the model to generate the optimal, unbiased estimate of magnitude image which is used for loss calculation. For denoised MRS reconstruction, we use ℓ_1 loss following the previous practice[30] so the loss is

$$\mathcal{L}^{denoise} = \mathcal{L}^{\ell_1}(\Re(x), \Re(y)) + \mathcal{L}^{\ell_1}(\Im(x), \Im(y)) \quad (17)$$

Data consistency is applied after each RACUNet and AFT block so that the known positions of output data are replaced by the original data samples to get better fidelity[31].

3.4. Experimental data

Two datasets were used in this study: a complex-valued normal-field human brain MRI dataset from the fastMRI dataset[22] and a complex-valued human brain MRS dataset from the Big GABA dataset[23]. The proposed methods were trained on these datasets separately.

The normal-field human brain MRI dataset contains fully sampled brain MRIs obtained on 3 and 1.5 Tesla magnets. We selected 4-channels axial T1-weighted and T2-weighted scans from the raw fastMRI dataset. A total number of 943 scans were used with 794, 99, and 50 each for the training, validation, and test set. All the scans were first normalized to the max intensity value of one and cropped to 640×320 matrix size.

The human brain MRS dataset contains GABA-edited MEGA-PRESS data obtained on 3T Philips scanners from different sites. Each subject was scanned for 320 averages (160 ON and 160 OFF repetitions). The data points acquired by each repetition is 2048. A total number of 101 scans were selected from the Big GABA dataset with 80, 10, and 11 each for the

training, validation, and test set. All the scans were first normalized to the max spectra magnitude value of one.

During the accelerated MRI reconstruction, all the k-space data was undersampled from the fully sampled k-space by applying a mask in the phase-encoding direction. We use the acceleration rate (or acceleration factor), to denote the level of scan time reduced for the undersampled k-space data, which is defined as the ratio of the amount of k-space data required for a fully sampled image to the amount collected in an undersampled k-space data[32]. The sampling ratio, SR, is also used to denote the information retained in the undersampled k-space data, which is defined as the inverse of the acceleration rate. An equispaced mask with approximate acceleration matching is used to undersample the k-space data. The fraction of low-frequency columns to be retained for acceleration rates 2x, 4x, and 8x are 16%, 8%, and 4% respectively.

During the denoised MRS reconstruction, we use the reduction rate, R, to denote the noise level, which is defined as the ratio of the number of total repetitions (160 for this study) to the number of repetitions retained for a noisy input. We generate the noisy FIDs with 5 reduction rates of 10, 20, 40, 80, and 160.

3.5. Measurement of Reconstruction Quality

Three metrics were adopted for the quantitative evaluation of the image quality compared with the ground truth: structural similarity (SSIM)[33], peak signal-to-noise ratio (PSNR), and normalized root mean squared error (NRMSE). For the quality measurement of the 1D spectra, another three metrics were used: Pearson correlation coefficient (PCC), Spearman’s rank correlation coefficient (SCC), and goodness-fitting coefficient (GFC)[34]. The GFC is introduced to evaluate the goodness of the mathematical reconstruction with a value ranging from 0 to 1, where 1 indicates a perfect reconstruction. If \hat{y}_i is the predicted value of the i -th sample and y_i is the corresponding true value, then the GFC estimated over n_{samples} is defined as

$$\text{GFC}(y, \hat{y}) = \frac{|\sum_{i=0}^{n_{\text{samples}}-1} y_i \hat{y}_i|}{|\sum_{i=0}^{n_{\text{samples}}-1} y_i^2|^{1/2} |\sum_{i=0}^{n_{\text{samples}}-1} \hat{y}_i^2|^{1/2}}. \quad (18)$$

4. Results

4.1. Comparison study

The effectiveness of the AFTNet was evaluated on the test set of the human normal-field MRI dataset through a comparative study as shown in Figure 4, where the up row shows the visualization of the baseline models, including conventional Fourier transform-based networks and score-MRI. The bottom row shows the proposed networks and ground truth derived from the fully-sampled k-space data. Both the residual maps against the ground truth and the zoomed-in areas are presented. The residual maps are normalized to the max value of 0.5 such that they are comparable across all models. We first compare the AFT-only network with the results after DFT. It clearly shows that the light trainable AFT block not only approximates the DFT but also facilitates artifact removal with the presence of signal non-ideality. Comparing the results of the AFT-only network and score-MRI, which solves the image reconstruction inverse problem based on score-based generative models, we demonstrate that even with such a simple structure, AFT can achieve similar performance in terms of PSNR and NRMSE. The score-MRI was originally trained on the knee dataset and we fine-tuned it on our dataset. Qualitatively, AFTNet outperformed score-MRI, as can be seen from the difference magnitude map and zoomed-in area in Figure 4 by comparing the results of AFTNet and score-MRI. The quantitative metrics demonstrate the superior performance of AFTNet over score-MRI, as shown in Table 1, including the SSIM, PSNR, and NRMSE across all acceleration rates. The statistical t-test between the metrics of score-MRI and AFTNet also shows the superior accelerated reconstruction of the proposed method with a p-value under 0.0001. Furthermore, the AFT block can serve as a better replacement for DFT by comparing the results of DFTNet and AFTNet, where all AFTNet shows better performance than the DFTNet, as can be seen from the residual maps. It should be pointed out that AFTNet-KI significantly outperforms DFTNet-KI, indicating that AFT can be implemented to connect two networks while preserving the capability of both networks.

4.2. Ablation study

Different structures of AFTNet, as mentioned in Section 3.2, were compared under datasets with different field strengths and different modalities to verify the stability and generality of the AFTNet. In addition, the effectiveness of the front-end/back-end convolutional networks is also evaluated in

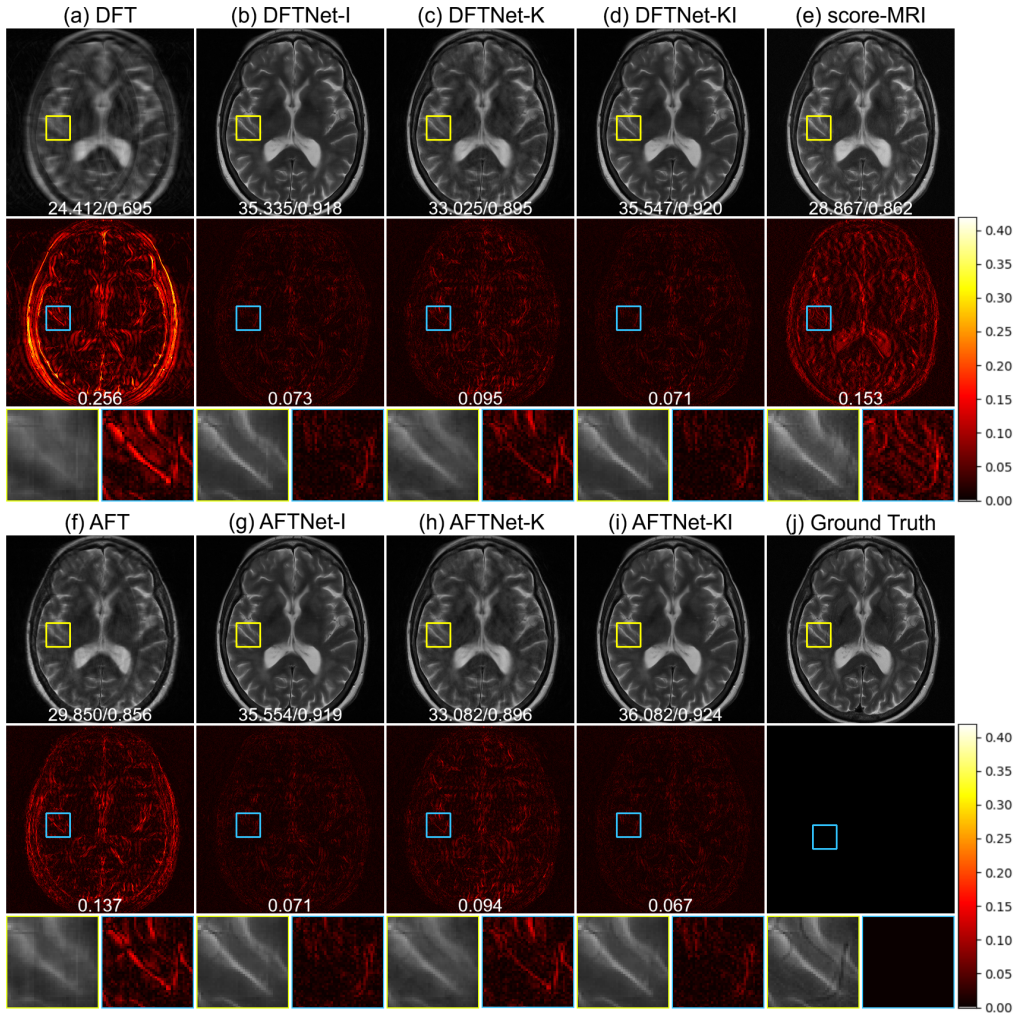


Figure 4: Comparison between baseline methods and AFTNet. Here we present the qualitative results under 4x acceleration rate, where a 1D 4x equal-spaced sampling mask with 8% of low-frequency columns retained is implemented to undersample the input k-space data. Residual map shows the difference magnitude against ground truth (in Hot colormap). Yellow and blue boxes show the zoomed-in version of the indicated area. White numbers in the magnitude images indicate PSNR (dB) and SSIM. White numbers in the residual maps indicate NRMSE.

this section. To validate the robustness of AFTNet to k-space artifacts, these proposed AFTNet structures were compared on the image reconstruction and accelerated reconstruction as described in Section 3.4. Furthermore, the extended AFTNet was compared with numerical methods using 1-dimensional MRS FID data on the denoised reconstruction.

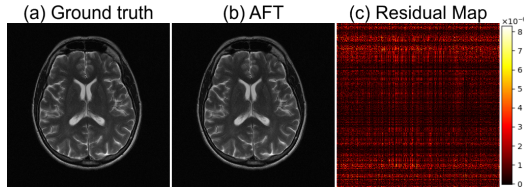


Figure 5: Human 1.5/3T MRI reconstruction results. (a) Ground truth, (b) proposed method, (c) difference magnitude of (a) and (b) (in Hot colormap).

First, we show the results of human 1.5/3T MRI reconstruction using raw fully-sampled fastMRI k-space data in Figure 5. All the images shown here and in the following sections are cropped so that the anti-aliasing placed outside the field of view (FOV) in phase-encoding directions is removed. The ground truth image is derived by applying conventional Fourier transformation to the k-space data. It can be seen that the ground truth image obtained from FT is identical to the AFT prediction, which human observers can not distinguish. The results adhere to the mathematical description we discussed in Section 2.1. The residual map (pixel-wise difference between the ground truth image and the AFT prediction) shows that no brain structural information is presented. The grid-like remaining error is mainly caused by precision loss during floating-point calculation in matrix multiplication.

In Figure 4, we show the results of human 1.5/3T accelerated reconstruction using under-sampled fastMRI k-space data. In the first row, we see the reconstructions from 1D 4x equal-spaced sampling, in which 8% of low-frequency columns are retained. Here, we compare different AFTNet structures with the zero-filling method. AFTNet-KI performs outstanding reconstruction, where less structural difference can be seen from the residual map in the second row. The third row shows zoomed-in areas of both images and residual maps. AFTNet-I produces a more blurry reconstruction which loses the structural details. Reconstruction through AFTNet-K induces foggy artifacts, which is reflected in terms of SSIM. Figure 6 shows the accelerated reconstruction results by comparing AFT and AFTNet (I, K, and KI) to their counterparts in terms of SSIM across acceleration rates 2x,

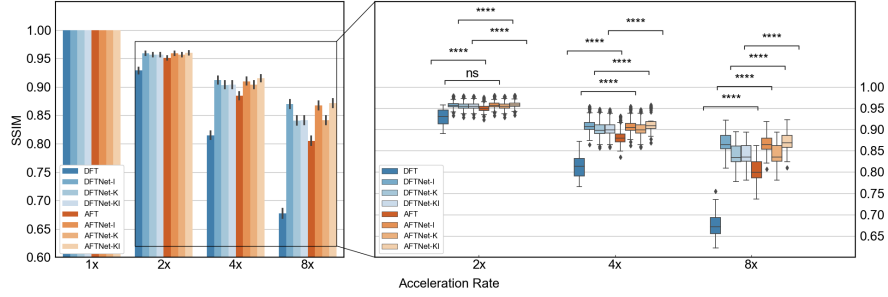


Figure 6: Results of human 1.5/3T MRI accelerated reconstruction by comparing AFTNet (K Model, I Model, and KI Model) and with their DFT counterparts in terms of SSIM for acceleration rates 1x, 2x, 4x, and 8x. p-values indicate results from two-sided t-tests for paired samples between the DFT-based model and AFT-based model. (ns: $p > 0.05$, *: $p \leq 0.05$, **: $p \leq 0.01$, ***: $p \leq 0.001$, ****: $p \leq 0.0001$)

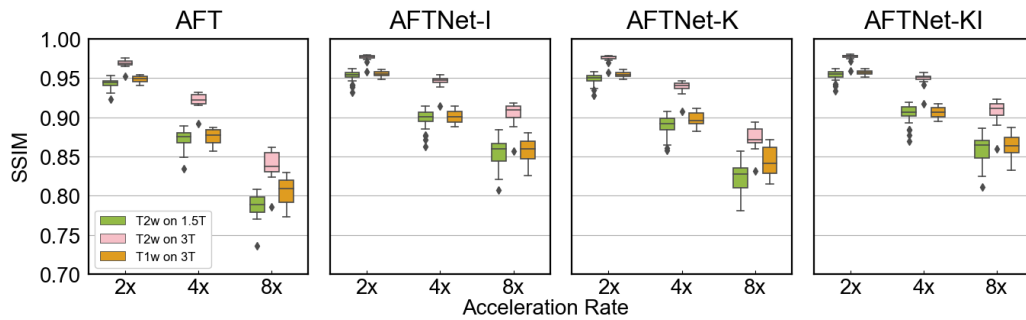


Figure 7: Results of human 1.5/3T MRI accelerated reconstruction by comparing AFTNet (I Model, K Model, and KI Model) in terms of SSIM on different acquisition types and system field strength for acceleration rates 2x, 4x, and 8x.

4x, and 8x. The performance of DFT drops linearly as the acceleration rate increases while the AFTNet methods are more robust to the acceleration scale. The t-test between AFT-based and DFT-based structures indicates that the AFTNet overcomes all DFTNet structures significantly except for the I model in the 2x acceleration rate. The results of AFTNet on different acquisition types and system field strength in Figure 7 demonstrate that higher system field strength yields better reconstruction which is due to the original imaging quality between different fields and the reconstruction on T2w images performs better than that on T1w images.

A comprehensive comparison of quantitative metrics on the test set is provided in Table 1 and Table 2 for accelerated reconstruction. AFTNet-KI outperforms other AFTNet structures on all the different acceleration rates and both AFTNet-KI and AFTNet-I perform significantly better than other AFTNet-K structures. Table 2 shows detailed quantitative metrics of human 1.5/3T MRI accelerated reconstruction results grouped by image contrast and system field strength. It is worth mentioning that although AFTNet-K does not outperform other AFTNet structures in the accelerated reconstruction task, it demonstrates the ability to learn in a sparse frequency domain and its sparse representations with a complex-valued convolutional network.

4.3. Human normal-field MRS study

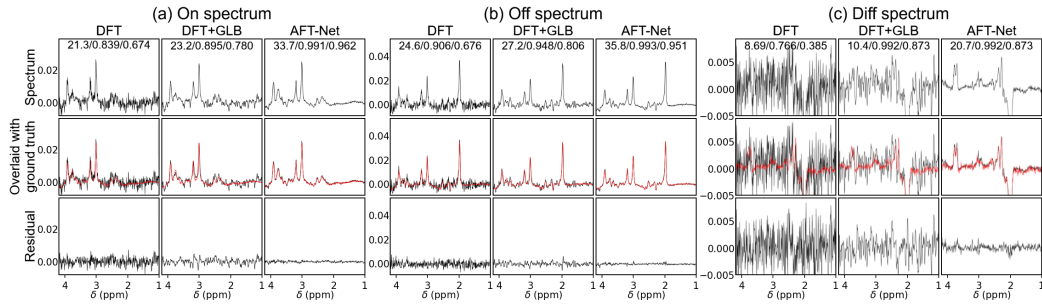


Figure 8: Human 3T MRS denoised reconstruction results. The acceleration rate is 80 for each spectrum. (a) Reconstruction results for the ON spectrum, (b) reconstruction results for the OFF spectrum, and (c) results for the DIFF spectrum derived from (a) and (b). 1st row: reconstructed spectra, 2nd row: reconstructed spectra overlaid with ground truth (in red line), 3rd row: Difference of reconstructed spectra against ground truth. Black numbers in the upper center location indicate PSNR (db), PCC, and SCC, respectively.

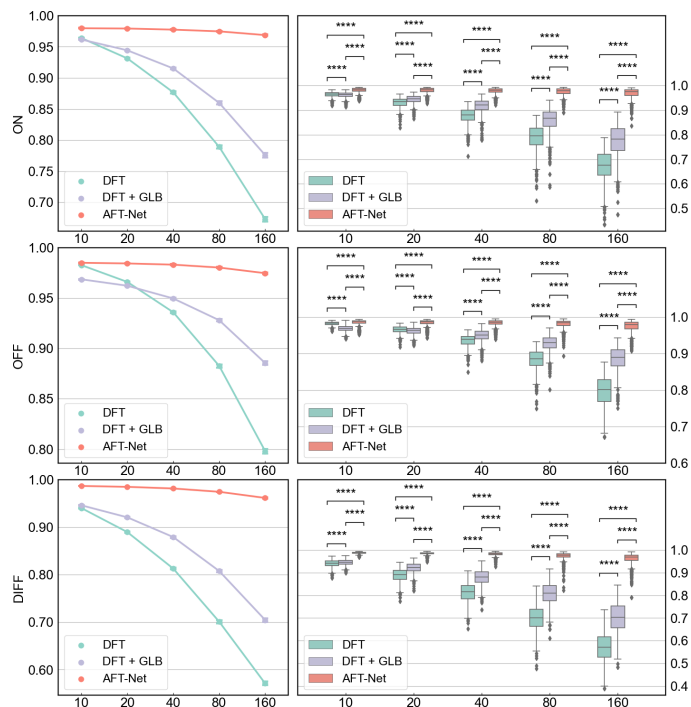


Figure 9: Results of human 3T MRS denoised reconstruction by comparing AFTNet (I Model), DFT, and DFT with Gaussian line broadening in terms of GFC. p-values indicate results from two-sided t-tests for paired samples. (ns: $p > 0.05$, *: $p \leq 0.05$, **: $p \leq 0.01$, ***: $p \leq 0.001$, ****: $p \leq 0.0001$)

Magnetic resonance spectroscopy, namely MRS, is widely used for measuring human metabolism. While MRS has the potential to be highly valuable in clinical practice, it poses several challenges such as low signal-to-noise ratio, overlapping metabolite signals, experimental artifacts, and long acquisition times. Here, the AFTNet is leveraged as a unified MRS reconstruction approach, which aims to reconstruct and process the FID in parallel, as shown in Figure 8.

We trained our model on the MEGA-PRESS spectra from the Big GABA dataset for two reasons. First, as a proof of concept study, to guarantee the convergence of the supervised learning task, we need the dataset to be sufficient in the number of samples, good in data quality, and publicly available. Thus the Big GABA dataset perfectly meets our requirements. Second, the smaller targeted signals are revealed by the subtraction of 2 spectra containing strong signals (OFF and ON), which provide a good way to verify the performance of the proposed method by measuring the subtraction artifacts. A total number of 101 subjects acquired by the Philips scanners were used in the training. For each subject, a standard GABA ON/OFF edited MRS acquisition was run, where ON editing pulses were placed at 1.9 ppm and OFF editing pulses were placed at 7.46 ppm. The acquisition number is 320 (160 ON and 160 OFF transients) per subject. The AFTNet was trained with an input size of 2048. The ground truth of the ON/OFF spectra is derived by taking the average over 160 acquisitions. We denote the ground truth as noiseless signals. For the training, we combined randomly sampled acquisitions of each subject to retrieve a noisy signal. By decreasing/increasing the number of sampled acquisitions, we can generate signals with higher/lower noise. We use the reduction rate (R) to denote the level of noise, which is defined as the ratio of the total acquisition number and the number of acquisitions sampled. This quantity is very handy to assess the power of denoising methods in practical terms. Retrieving accurate denoised signals at a high R has implications for the potential reduction of total experimental time.

The results of the AFTNet approach and conventional numerical methods with Gaussian line broadening are illustrated in Figure 9. The first row shows the reconstructed spectrum from the numerical methods and the proposed AFTNet. The second row indicates the reconstructed spectrum overlaid with the ground truth. The third row plots the difference between the reconstructed spectrum and the ground truth. Under a reduction rate of 80, where only 2 acquisitions were used over all 160 acquisitions, the AFTNet shows excellent performance at high reduction rates. The AFTNet outperforms

other methods for the DIFF spectra, indicating that the AFTNet removes the noise in the FIDs while preserving the subject-level features. We used the Goodness-of-Fit Coefficient (GFC) to measure the similarity between the reconstructed spectra and the ground truth, as shown in the Table 3. The metric value increases as the reduction rate decreases, but the absolute difference between high and low reduction rates is tiny (0.9798 for OFF spectra under a reduction rate of 10 vs. 0.9688 for OFF spectra under a reduction rate of 160). In addition, AFTNet outperforms the DFT+GLB (Gaussian Line Broadening) method across all metrics in the table.

5. Discussion

In this study, a unified MR image reconstruction framework is proposed, which is composed of two main components: artificial Fourier transform block and complex-valued residual attention U-Net. The AFT block is used to approximate the conventional DFT, which is demonstrated in Table 1 and proofed in Section 3.1. The front-end/back-end convolutional layers are used to extract features at different levels in the k-space/image domains and play different roles in various tasks. As shown in Table 1, both front-end and back-end convolutional layers show superior accelerated reconstruction performance under all sampling ratios compared with single front-end/back-end convolutional layers. This is potentially because the undersampling is performed in k-space where the artifacts are separated from the non-artifact. While in the image domain, it is converted to aliasing overlapped over the whole image. The artifacts removal task can be recast as an image inpainting problem in the k-space domain which can be done more easily by the front-end convolutional layers. However, all the structures with front-end-only convolutional layers show lower performance, indicating that the sparse representation of k-space data makes it harder for a convolutional network to extract noise information in the low-frequency areas and back-end convolutional layers are necessary to achieve the optimal performance.

Domain-transform manifold learning has been introduced for years and several deep learning frameworks were developed based on this idea. The first model, AUTOMAP[11], proposed the simple FC-Conv structure which can only be applied to images with small matrix size due to its redundant FC layers. DOTA-MRI[13] extended AUTOMAP to Conv-FC-Conv structure and applied FC layers to only one dimension (phase-encoding direction). However, it did not extend the model structure and implement end-to-end

complex-valued neural networks. The AFTNet we proposed in this study solves the problem mentioned above through a modular-designed AFT block. We also demonstrated that the extended AFTNet can also be applied to 1D data in Section 4.3. In addition, previous works define the loss in the magnitude image, while we calculate the loss in the complex-valued image domain, which preserves the relations between the real and imaginary parts. The phase is then derived from the output of AFTNet, which is essential for several phase-based applications, such as flow quantification and fat–water separation.

Complex-valued neural networks, especially complex-valued convolutional networks[21, 20], have been studied for MRI reconstruction but they mainly focused on simple tasks or only applied it to the image domain. We investigate the different impacts of complex-valued convolutional networks on the k-space and image domain and extend the application to accelerated reconstruction and denoised reconstruction, which are more clinically important. We also incorporate domain-manifold learning by adding domain transform blocks which determine the mapping between the k-space and image domain instead of conventional discrete Fourier transform. It is more robust to noise and signal nonideality due to imperfect acquisition. We also extend the application of complex-valued convolutional networks to 1D MRS denoised reconstruction, which has not been studied in previous work.

One remaining methodological limitation is that the FC layers used by AFTNet narrow the application to datasets with various image matrix sizes. Although the convolutional layers are not sensitive to the image matrix sizes and cropping/padding can be applied to match the desired sizes, the features of FC layers need to be selected carefully which requires further investigation. Another parameter that needs to be taken into account is the coil number. In this study, we selected especially 4-channel MRI data for convenience of data preprocessing. While deep learning-based coil combinations could be incorporated into the framework in future work. Furthermore, diffusion models are shown to be a powerful tool for image reconstruction across body regions and coil numbers[14]. However, the score-MRI we compared in this study does not demonstrate superior performance compared with AFTNet and the inference stage time is extremely long. This is potential because the backbone of the score-MRI is still a real-valued U-Net like structure and the relation between the real and imaginary part is not considered during the calculation of the score function. For future works, the AFTNet could be further extended by leveraging diffusion-based models with complex-valued

convolutional networks as the backbone and careful optimization to reduce the inference time.

6. Conclusion

In conclusion, we propose AFT, a novel artificial Fourier transform framework that determines the mapping between k-space and image domain as conventional DFT while having the ability to be fine-tuned/optimized with further training. The flexibility of AFT allows it to be easily incorporated into any existing deep learning network as learnable or static blocks. We then utilized AFT to design our AFTNet, which implements complex-valued U-Net to extract features in the k-space and/or image domain. We aim to combine reconstruction and acceleration/denoising tasks into a unified network that simultaneously enhances the image quality by removing artifacts directly from the k-space and/or image domain. The proposed methods are evaluated on datasets with additional artifacts, different contrasts, and different modalities. Our AFTNet achieves competitive results compared with other methods and proves to be more robust to noise and contrast differences. An extensive study on various system fields, various modalities, and various tasks demonstrates the effectiveness and generality of AFTNet.

References

- [1] G. Georgiou, C. Koutsougeras, Complex domain backpropagation, *IEEE Transactions on Circuits and Systems II: Analog and Digital Signal Processing* 39 (5) (1992) 330–334. doi:10.1109/82.142037.
- [2] N. Guberman, On complex valued convolutional neural networks, arXiv preprint arXiv:1602.09046 (2016).
- [3] C. Trabelsi, O. Bilaniuk, Y. Zhang, D. Serdyuk, S. Subramanian, J. F. Santos, S. Mehri, N. Rostamzadeh, Y. Bengio, C. J. Pal, Deep complex networks, in: *International Conference on Learning Representations*, 2018.
- [4] J. B. Johnson, Thermal agitation of electricity in conductors, *Physical review* 32 (1) (1928) 97.
- [5] H. Nyquist, Thermal agitation of electric charge in conductors, *Physical review* 32 (1) (1928) 110.

- [6] M. S. Hansen, P. Kellman, Image reconstruction: an overview for clinicians, *Journal of Magnetic Resonance Imaging* 41 (3) (2015) 573–585.
- [7] J. A. Fessler, Model-based image reconstruction for mri, *IEEE signal processing magazine* 27 (4) (2010) 81–89.
- [8] M. De Bruijne, *Machine learning approaches in medical image analysis: From detection to diagnosis* (2016).
- [9] J. W. Cooley, J. W. Tukey, An algorithm for the machine calculation of complex fourier series, *Mathematics of computation* 19 (90) (1965) 297–301.
- [10] D. Shen, G. Wu, H.-I. Suk, Deep learning in medical image analysis, *Annual review of biomedical engineering* 19 (2017) 221–248.
- [11] B. Zhu, J. Z. Liu, S. F. Cauley, B. R. Rosen, M. S. Rosen, Image reconstruction by domain-transform manifold learning, *Nature* 555 (7697) (2018) 487–492.
- [12] J. López-Randulfe, T. Duswald, Z. Bing, A. Knoll, Spiking neural network for fourier transform and object detection for automotive radar, *Frontiers in Neurorobotics* 15 (2021) 688344.
- [13] T. Eo, H. Shin, Y. Jun, T. Kim, D. Hwang, Accelerating cartesian mri by domain-transform manifold learning in phase-encoding direction, *Medical Image Analysis* 63 (2020) 101689.
- [14] H. Chung, J. C. Ye, Score-based diffusion models for accelerated mri, *Medical image analysis* 80 (2022) 102479.
- [15] K. Xu, M. Qin, F. Sun, Y. Wang, Y.-K. Chen, F. Ren, Learning in the frequency domain, in: *Proceedings of the IEEE/CVF conference on computer vision and pattern recognition*, 2020, pp. 1740–1749.
- [16] A. Hirose, *Complex-valued neural networks*, Vol. 400, Springer Science & Business Media, 2012.
- [17] A. Hirose, S. Yoshida, Generalization characteristics of complex-valued feedforward neural networks in relation to signal coherence, *IEEE Transactions on Neural Networks and learning systems* 23 (4) (2012) 541–551.

- [18] M. Tygert, J. Bruna, S. Chintala, Y. LeCun, S. Piantino, A. Szlam, A mathematical motivation for complex-valued convolutional networks, *Neural computation* 28 (5) (2016) 815–825.
- [19] O. Ronneberger, P. Fischer, T. Brox, U-net: Convolutional networks for biomedical image segmentation, in: *Medical Image Computing and Computer-Assisted Intervention–MICCAI 2015: 18th International Conference, Munich, Germany, October 5-9, 2015, Proceedings, Part III* 18, Springer, 2015, pp. 234–241.
- [20] D. Sikka, N. Igra, S. Gjerwold-Sellec, C. Gao, E. Wu, J. Guo, Cu-net: A completely complex u-net for mr k-space signal processing, in: *ISMRM (International Society of Magnetic Resonance Imaging) Virtual Conference & Exhibition, 2021, International Society of Magnetic Resonance Imaging (ISMRM).*, 2021.
- [21] E. Cole, J. Cheng, J. Pauly, S. Vasanawala, Analysis of deep complex-valued convolutional neural networks for mri reconstruction and phase-focused applications, *Magnetic resonance in medicine* 86 (2) (2021) 1093–1109.
- [22] J. Zbontar, F. Knoll, A. Sriram, T. Murrell, Z. Huang, M. J. Muckley, A. Defazio, R. Stern, P. Johnson, M. Bruno, et al., fastmri: An open dataset and benchmarks for accelerated mri, *arXiv preprint arXiv:1811.08839* (2018).
- [23] M. Mikkelsen, P. B. Barker, P. K. Bhattacharyya, M. K. Brix, P. F. Buur, K. M. Cecil, K. L. Chan, D. Y.-T. Chen, A. R. Craven, K. Cuypers, et al., Big gaba: Edited mr spectroscopy at 24 research sites, *Neuroimage* 159 (2017) 32–45.
- [24] S. Ioffe, C. Szegedy, Batch normalization: Accelerating deep network training by reducing internal covariate shift, in: *International conference on machine learning*, pmlr, 2015, pp. 448–456.
- [25] Y. Wu, K. He, Group normalization, in: *Proceedings of the European conference on computer vision (ECCV)*, 2018, pp. 3–19.
- [26] J. L. Ba, J. R. Kiros, G. E. Hinton, Layer normalization, *arXiv preprint arXiv:1607.06450* (2016).

- [27] D. P. Kingma, J. Ba, Adam: A method for stochastic optimization, arXiv preprint arXiv:1412.6980 (2014).
- [28] I. Loshchilov, F. Hutter, SGDR: stochastic gradient descent with warm restarts, in: 5th International Conference on Learning Representations, ICLR 2017, Toulon, France, April 24-26, 2017, Conference Track Proceedings, OpenReview.net, 2017.
URL <https://openreview.net/forum?id=Skq89Scxx>
- [29] P. B. Roemer, W. A. Edelstein, C. E. Hayes, S. P. Souza, O. M. Mueller, The nmr phased array, *Magnetic resonance in medicine* 16 (2) (1990) 192–225.
- [30] D. J. Ma, Y. Yang, N. Harguindeguy, Y. Tian, S. A. Small, F. Liu, D. L. Rothman, J. Guo, Magnetic resonance spectroscopy spectral registration using deep learning, *Journal of Magnetic Resonance Imaging* 59 (3) (2024) 964–975.
- [31] Z. Wu, W. Liao, C. Yan, M. Zhao, G. Liu, N. Ma, X. Li, Deep learning based mri reconstruction with transformer, *Computer Methods and Programs in Biomedicine* 233 (2023) 107452.
- [32] A. Deshmane, V. Gulani, M. A. Griswold, N. Seiberlich, Parallel mr imaging, *Journal of Magnetic Resonance Imaging* 36 (1) (2012) 55–72.
- [33] Z. Wang, E. P. Simoncelli, A. C. Bovik, Multiscale structural similarity for image quality assessment, in: *The Thrity-Seventh Asilomar Conference on Signals, Systems & Computers*, 2003, Vol. 2, Ieee, 2003, pp. 1398–1402.
- [34] J. Romero, A. Garcia-Beltrán, J. Hernández-Andrés, Linear bases for representation of natural and artificial illuminants, *JOSA A* 14 (5) (1997) 1007–1014.

Tables

Acc.	Metrics	Baseline				Ours			
		DFT	DFTNet-K	DFTNet-I	score-MRI	AFT	AFTNet-K	AFTNet-I	AFTNet-KI
1x	SSIM	-	1.000	1.000	1.000	1.000	1.000	1.000	1.000
	PSNR	-	153.3	153.3	63.9	153.3	153.3	153.3	153.3
	NRMSE	-	0.000	0.000	0.003	0.000	0.000	0.000	0.000
2x	SSIM	0.929	0.956	0.959	0.939	0.951	0.957	0.959	0.960****
	PSNR	33.6	38.9	39.5	38.5	37.0	38.9	39.6	39.8****
	NRMSE	0.105	0.057	0.053	0.052	0.070	0.057	0.052	0.051****
4x	SSIM	0.815	0.903	0.912	0.874	0.885	0.904	0.912	0.915****
	PSNR	27.3	33.7	35.2	32.8	32.0	33.7	35.3	35.7****
	NRMSE	0.214	0.104	0.086	0.099	0.125	0.103	0.085	0.082****
8x	SSIM	0.677	0.840	0.869	0.787	0.805	0.841	0.869	0.872****
	PSNR	23.8	29.4	31.3	27.5	27.6	29.4	31.3	31.5****
	NRMSE	0.32	0.171	0.135	0.189	0.208	0.171	0.137	0.132***

Table 1: Quantitative metrics of human 1.5/3T MRI accelerated reconstruction. Numbers are presented as mean value \pm standard deviation. Numbers in boldface indicate the best metric out of all the methods. Acc.: Acceleration Rate. p-values indicate results from two-sided t-tests for paired samples between best and second-best models. (ns: $p > 0.05$, *: $p \leq 0.05$, **: $p \leq 0.01$, ***: $p \leq 0.001$, ****: $p \leq 0.0001$)

(a) T2w images on 1.5T

Acc.	Metrics	DFT	Ours			
			AFT	AFTNet-K	AFTNet-I	AFTNet-KI
1x	SSIM	-	1.000 ± 0.000	1.000 ± 0.000	1.000 ± 0.000	1.000 ± 0.000
	PSNR	-	154.0 ± 1.3	154.0 ± 1.3	154.0 ± 1.3	154.0 ± 1.3
	NRMSE	-	0.000 ± 0.000	0.000 ± 0.000	0.000 ± 0.000	0.000 ± 0.000
2x	SSIM	0.911 ± 0.011	0.943 ± 0.008	0.948 ± 0.008	0.952 ± 0.008	0.953 ± 0.007
	PSNR	32.5 ± 1.1	36.5 ± 1.2	38.0 ± 1.3	39.1 ± 1.2	39.2 ± 1.2
	NRMSE	0.127 ± 0.008	0.080 ± 0.004	0.068 ± 0.005	0.060 ± 0.004	0.059 ± 0.005
4x	SSIM	0.792 ± 0.014	0.871 ± 0.013	0.890 ± 0.014	0.897 ± 0.014	0.903 ± 0.013
	PSNR	26.7 ± 1.0	31.7 ± 1.4	32.8 ± 1.3	35.0 ± 1.2	35.3 ± 1.2
	NRMSE	0.248 ± 0.015	0.141 ± 0.006	0.124 ± 0.007	0.095 ± 0.007	0.093 ± 0.007
8x	SSIM	0.662 ± 0.023	0.788 ± 0.016	0.823 ± 0.020	0.855 ± 0.019	0.859 ± 0.018
	PSNR	23.6 ± 1.1	27.0 ± 1.4	28.4 ± 1.5	30.9 ± 1.3	30.9 ± 1.3
	NRMSE	0.358 ± 0.022	0.240 ± 0.011	0.204 ± 0.010	0.153 ± 0.008	0.153 ± 0.009

(b) T2w images on 3T

Acc.	Metrics	DFT	Ours			
			AFT	AFTNet-K	AFTNet-I	AFTNet-KI
1x	SSIM	-	1.000 ± 0.000	1.000 ± 0.000	1.000 ± 0.000	1.000 ± 0.000
	PSNR	-	152.3 ± 1.2	152.3 ± 1.2	152.3 ± 1.2	152.3 ± 1.2
	NRMSE	-	0.000 ± 0.000	0.000 ± 0.000	0.000 ± 0.000	0.000 ± 0.000
2x	SSIM	0.948 ± 0.007	0.968 ± 0.006	0.975 ± 0.006	0.976 ± 0.006	0.976 ± 0.006
	PSNR	33.1 ± 1.1	36.6 ± 1.3	39.4 ± 1.5	40.2 ± 1.5	40.4 ± 1.6
	NRMSE	0.093 ± 0.009	0.063 ± 0.006	0.046 ± 0.006	0.042 ± 0.006	0.041 ± 0.006
4x	SSIM	0.841 ± 0.021	0.921 ± 0.011	0.937 ± 0.011	0.945 ± 0.010	0.948 ± 0.010
	PSNR	26.7 ± 1.2	31.1 ± 1.3	33.3 ± 1.4	35.2 ± 1.4	35.5 ± 1.5
	NRMSE	0.195 ± 0.017	0.117 ± 0.007	0.091 ± 0.006	0.074 ± 0.008	0.071 ± 0.008
8x	SSIM	0.694 ± 0.031	0.838 ± 0.021	0.872 ± 0.017	0.903 ± 0.017	0.906 ± 0.017
	PSNR	23.1 ± 1.3	26.6 ± 1.3	28.2 ± 1.3	30.5 ± 1.2	30.7 ± 1.3
	NRMSE	0.295 ± 0.022	0.198 ± 0.011	0.164 ± 0.009	0.126 ± 0.010	0.124 ± 0.010

(c) T1w images on 3T

Acc.	Metrics	DFT	Ours			
			AFT	AFTNet-K	AFTNet-I	AFTNet-KI
1x	SSIM	-	1.000 ± 0.000	1.000 ± 0.000	1.000 ± 0.000	1.000 ± 0.000
	PSNR	-	153.0 ± 0.8	153.0 ± 0.8	153.0 ± 0.8	153.0 ± 0.8
	NRMSE	-	0.000 ± 0.000	0.000 ± 0.000	0.000 ± 0.000	0.000 ± 0.000
2x	SSIM	0.941 ± 0.006	0.949 ± 0.004	0.955 ± 0.004	0.956 ± 0.004	0.957 ± 0.003
	PSNR	35.8 ± 0.7	38.3 ± 0.7	40.0 ± 0.8	40.1 ± 0.9	40.4 ± 0.8
	NRMSE	0.079 ± 0.008	0.059 ± 0.004	0.048 ± 0.003	0.048 ± 0.004	0.046 ± 0.003
4x	SSIM	0.830 ± 0.014	0.875 ± 0.010	0.898 ± 0.009	0.901 ± 0.008	0.906 ± 0.008
	PSNR	28.9 ± 0.7	33.2 ± 0.8	35.7 ± 0.9	35.9 ± 1.1	36.4 ± 1.0
	NRMSE	0.174 ± 0.020	0.106 ± 0.008	0.080 ± 0.006	0.077 ± 0.009	0.073 ± 0.007
8x	SSIM	0.687 ± 0.024	0.805 ± 0.019	0.844 ± 0.019	0.858 ± 0.016	0.863 ± 0.015
	PSNR	24.7 ± 0.9	29.5 ± 0.8	32.1 ± 0.9	33.0 ± 1.3	33.3 ± 1.2
	NRMSE	0.281 ± 0.027	0.162 ± 0.013	0.121 ± 0.009	0.109 ± 0.015	0.104 ± 0.013

Table 2: Quantitative metrics of human 1.5/3T MRI accelerated reconstruction. Numbers are presented as mean value \pm standard deviation. Numbers in boldface indicate the best metric out of all the methods.

R	Spectrum	DFT	DFT+GLB	AFTNet
10	ON	0.9827 \pm 0.0047	0.9686 \pm 0.0086	0.9850 \pm 0.0085
	OFF	0.9641 \pm 0.0104	0.9617 \pm 0.0108	0.9798 \pm 0.0124
	DIFF	0.9403 \pm 0.0164	0.9461 \pm 0.0126	0.9868 \pm 0.0037
20	ON	0.9660 \pm 0.0090	0.9622 \pm 0.0111	0.9843 \pm 0.0092
	OFF	0.9314 \pm 0.0192	0.9443 \pm 0.0170	0.9794 \pm 0.0127
	DIFF	0.8897 \pm 0.0283	0.9208 \pm 0.0206	0.9849 \pm 0.0055
40	ON	0.9359 \pm 0.0162	0.9496 \pm 0.0155	0.9831 \pm 0.0098
	OFF	0.8768 \pm 0.0318	0.9152 \pm 0.0281	0.9776 \pm 0.0139
	DIFF	0.8129 \pm 0.0418	0.8792 \pm 0.0325	0.9815 \pm 0.0078
80	ON	0.8826 \pm 0.0280	0.9280 \pm 0.0214	0.9803 \pm 0.0120
	OFF	0.7890 \pm 0.0486	0.8598 \pm 0.0452	0.9748 \pm 0.0160
	DIFF	0.7010 \pm 0.0566	0.8077 \pm 0.0480	0.9745 \pm 0.0154
160	ON	0.7981 \pm 0.0403	0.8854 \pm 0.0325	0.9747 \pm 0.0160
	OFF	0.6730 \pm 0.0619	0.7759 \pm 0.0638	0.9688 \pm 0.0200
	DIFF	0.5710 \pm 0.0654	0.7047 \pm 0.0662	0.9616 \pm 0.0245

Table 3: GFC metric of human 3T MRS denoised reconstruction. Numbers are presented as mean value \pm standard deviation. Numbers in boldface indicate the best metric out of all the methods.